https://doi.org/10.1016/j.ultrasmedbio.2017.09.003

● *Original Contribution*

SPATIAL ANGULAR COMPOUNDING TECHNIQUE FOR H-SCAN ULTRASOUND IMAGING

Mawia Khairalseed,*† Fangyuan Xiong,*‡ Jung-Whan Kim,§ Robert F. Mattrey,¶
Kevin J. Parker,‖ and Kenneth Hoyt*¶

* Department of Bioengineering, University of Texas at Dallas, Richardson, Texas, USA; † Department of Biomedical Engineering,
Sudan University of Science and Technology, Khartoum, Sudan; ‡ Department of Medical Ultrasound, Tongji Hospital of the Tongji
Medical College, Huazhong University of Science and Technology, Wuhan, China; § Department of Biological Sciences, University
of Texas at Dallas, Richardson, Texas, USA; ¶ Department of Radiology, University of Texas Southwestern Medical Center, Dallas,
Texas, USA; and ‖ Department of Electrical and Computer Engineering, University of Rochester, Rochester, New York, USA

Abstract—H-Scan is a new ultrasound imaging technique that relies on matching a model of pulse-echo formation to the mathematics of a class of Gaussian-weighted Hermite polynomials. This technique may be beneficial in the measurement of relative scatterer sizes and in cancer therapy, particularly for early response to drug treatment. Because current H-scan techniques use focused ultrasound data acquisitions, spatial resolution degrades away from the focal region and inherently affects relative scatterer size estimation. Although the resolution of ultrasound plane wave imaging can be inferior to that of traditional focused ultrasound approaches, the former exhibits a homogeneous spatial resolution throughout the image plane. The purpose of this study was to implement H-scan using plane wave imaging and investigate the impact of spatial angular compounding on H-scan image quality. Parallel convolution filters using two different Gaussian-weighted Hermite polynomials that describe ultrasound scattering events are applied to the radiofrequency data. The H-scan processing is done on each radiofrequency image plane before averaging to get the angular compounded image. The relative strength from each convolution is color-coded to represent relative scatterer size. Given results from a series of phantom materials, H-scan imaging with spatial angular compounding more accurately reflects the true scatterer size caused by reductions in the system point spread function and improved signal-to-noise ratio. Preliminary *in vivo* H-scan imaging of tumor-bearing animals suggests this modality may be useful for monitoring early response to chemotherapeutic treatment. Overall, H-scan imaging using ultrasound plane waves and spatial angular compounding is a promising approach for visualizing the relative size and distribution of acoustic scattering sources. (E-mail: kenneth.hoyt@utdallas.edu)   © 2018 World Federation for Ultrasound in Medicine & Biology. All rights reserved.

Key Words: Acoustic scatterers, H-Scan, Plane waves, Spatial angular compounding, Tissue characterization, Ultrasound.

INTRODUCTION

The conventional gray-scale ultrasound image is constructed from the backscatter signal following transmission of a short acoustic pulse. This backscatter radiofrequency (RF) signal is composed of specular reflections of ultrasound waves at tissue boundaries and by diffusive scattering from small irregularities within tissue (Szabo 2014). Note that scattering in the latter regime has important implications in ultrasound imaging as tissue is often modeled as

an ensemble of small point scatterers. Lastly, the envelope of these backscattered signals is processed before being displayed in real time for visualizing deep tissue anatomic structures.

The use of ultrasound for quantitative tissue characterization has been an exciting research prospect for several decades. Herein, the challenge is to find hidden patterns in the ultrasound data to reveal more information on tissue function and pathology than seen in conventional ultrasound images (Thijssen 1989). To that end, several different tissue characterization methods have been introduced, including backscatter classification (Chen et al. 1993; Madsen et al. 1984), integrated backscatter (Thomas et al. 1989), spectral feature extraction (Bridal et al. 1996; Hall et al.

Address correspondence to: Kenneth Hoyt, University of Texas at Dallas, BSB 13.929, 800 West Campbell Road, Richardson, TX 75080, USA. E-mail: kenneth.hoyt@utdallas.edu

1997; Kolios et al. 2002; Lizzi et al. 1997; Oelze and O'Brien 2002; Romijn et al. 1989) and, more recently, tissue elasticity imaging (Doherty et al. 2013; Gennisson et al. 2013; Hoyt et al. 2006, 2008a, 2008b; Parker et al. 2011). A limitation of many tissue characterization methods is that they require a complicated calibration step before measurement or use of a relatively large kernel of ultrasound data during quantification, which negatively affects spatial resolution.

Bypassing some of the limitations associated with traditional tissue characterization approaches, a new modality has emerged for ultrasound classification of acoustic scatterers (Parker 2016a, 2016b). Termed H-scan (where the "H" denotes Hermite), this ultrasound technique relies on matching a model of image formation to the mathematics of a class of Gaussian-weighted Hermite polynomials (GWHPs). As further detailed by Parker (2016a, 2016b), H-scan classifies echoes according to their frequency weighting using GWHP-matched filters. It does not extract other intrinsic backscatter spectral measures, as does quantitative ultrasound (Oelze and Mamou 2016; Szabo 2014); however, H-scan does not require ensemble averaging over regions and has spatial resolution comparable to that of the intrinsic axial resolution of the imaging system. Nonetheless, because current H-scan techniques use focused ultrasound data acquisitions, spatial resolution degrades away from the focal region and inherently affects relative scatterer size estimation compared with plane wave imaging, which instantaneously exposes the entire image field with nearly uniform acoustic intensity, with the exception of depth-dependent attenuation that can be corrected for, in part, by using time-gain compensation. The resolution of ultrasound plane wave imaging can be inferior to that of traditional focused ultrasound approaches; the former exhibits homogeneous spatial resolution throughout the image plane that can be improved through spatial angular compounding (Couture et al. 2012; Tanter and Fink 2014).

In this article, we detail development of a new H-scan technology implemented on a programmable ultrasound system that integrates both plane wave imaging and spatial angular compounding to improve scatterer size estimation (*i.e.*, tissue characterization) as validated using a series of *in vitro* and *in vivo* studies.

THEORY

During ultrasound imaging, the backscattered ultrasound signal $e(t)$ can be modeled as (Macovski 1983):

$$e(t) = A\{d(t) *** R(x, y, z)\} \qquad (1)$$

where A is a signal amplitude constant, $R(x,y,z)$ is the 3-D pattern of acoustic reflectors or scattering objects in the medium and $d(t)$ is the transducer impulse response defined

as the product of the propagating ultrasound pulse in the axial direction, $p(t)$, and beam pattern, $s(x,y)$. The symbol *** represents 3-D convolution.

Classification of ultrasound scattering

For the context of H-scan imaging, we briefly consider three simple types of acoustic scattering objects with an assumption of small spatial variations in medium density and compressibility. A more detailed overview of the H-scan format for classification of ultrasound scattering can be found in Parker (2016a, 2016b).

Large layer

This classification occurs when the scattering object is large compared with the wavelength of the propagating ultrasound pulse. The reflection process can be approximated as an incident ray with the scattered wavefronts following the shape of the object. The large layer has an interface that looks like a step function $u(z-z_o)$ of acoustic impedance Z at position z_o. The acoustic impedance for the large layer Z_L is calculated as:

$$Z_L(z) = Z + \Delta Z u(z - z_o) \qquad (2)$$

The reflection coefficient R_L is then related to the spatial derivative of Z_L by:

$$R_L(z) = \frac{1}{2Z}\left\{\frac{dZ_L(z)}{dz}\right\} = \frac{\Delta Z}{2Z}\delta(z - z_o) \qquad (3)$$

where $\delta(z-z_o)$ is the Dirac delta function at position z_o. The received signal is then the 1-D convolution * of the propagating ultrasound pulse $p(t)$ with the reflection coefficient at the large interface:

$$e_L(t) = p(t) * R_L(z) = \frac{\Delta Z}{2Z}p(t - t_o) \qquad (4)$$

Thin layer

This type of material has acoustic impedance that resembles a delta function $\delta(z-z_o)$ as:

$$Z_T(z) = Z + \Delta Z \delta(z - z_o) \qquad (5)$$

The reflection coefficient of the thin layer $R_T(z)$ is then given as the spatial derivative of Z_T:

$$R_T(z) = \frac{\Delta Z}{2Z}\left\{\frac{dZ_T(z)}{dz}\right\} = \frac{\Delta Z}{2Z}p\delta''(t - t_0) \qquad (6)$$

The received signal is then the convolution of the propagating ultrasound pulse and reflection coefficient of the thin layer:

$$e_T(t) = p(t) * R_T(z) = \frac{\Delta Z}{2Z}p'(t - t_o) \qquad (7)$$

Rayleigh scatterers

Rayleigh scattering occurs when the scattering object is smaller than the ultrasound wavelength. By use of the Born approximation, a small spherical scatterer creates a reflection that has pressure dependence with a frequency-squared weighting. This is an important relation because Fourier transform theorems state that frequency-squared weighting is equivalent to convolution with $\delta''(\cdot)$. Therefore, the reflection coefficient for a single Rayleigh scatterer or cloud of scatterers can be approximated by the formula (Parker 2016a):

$$e_S(t) = \frac{\Delta Z}{2Z} p''(t - t_0). \tag{8}$$

Note that the important distinction between the three classes of ultrasound scattering events detailed in eqns (4), (7) and (8) is in their relation to the transmitted ultrasound pulse and its derivatives in the propagation direction. In all three classes of reflectors, the echogenicity on B-scan and H-scan is directly proportional to ΔZ, the change in acoustic impedance.

In practice, one may wish to discriminate between different-sized scatterers yet the size sensitivity of H-scan classifications is not explicitly detailed in eqns (2) to (8). However, it should be noted that in scattering theory, there is a change in backscatter as a function of acoustic frequency that transitions form the long-wavelength limit (Rayleigh scattering, frequency squared weighting) to the short-wavelength limit (approaching specular reflection), and these changes cause shifts in the H-scan statistics. The specific details of this transition are beyond the scope of this article and left for future work.

Gaussian-weighted Hermite polynomials

Successive differentiation of a Gaussian pulse, $G(t) = e^{-t^2}$, generates the nth-order Hermite polynomials, which are defined by the formula (Poularikas 2010):

$$H_n(t) = (-1)^n e^{t^2} \frac{d^n}{dt^n} G(t) \tag{9}$$

$$n = 0, 1, 2, \ldots; \quad -\infty < t < \infty$$

GWHPs can then be generated by multiplying eqn (9) by $G(t)$. In practice, these GWHPs can be used as bandpass filters to isolate select frequency information. In fact, the $GH_4(t)$ function resembles a typical broadband ultrasound pulse (Parker 2016a). Assuming a pulse-echo system has a round trip impulse response of $p(t) = A_0 GH_4(t)$, then eqns (4), (7) and (8) can be approximated as:

$$e_L(t) = A_0 \frac{\Delta Z}{2Z} GH_4(t)(t - t_o) \tag{10}$$

$$e_T(t) = A_0 \frac{\Delta Z}{2Z} GH_5(t)(t - t_o) \tag{11}$$

$$e_S(t) = A_0 \frac{\Delta Z}{2Z} GH_6(t)(t - t_o) \tag{12}$$

respectively, where A_o is an amplitude scaling constant.

During ultrasound imaging, the received signals from a scattering medium can therefore be classified by their similarity to either $GH_4(t)$, $GH_5(t)$ or $GH_6(t)$. To monopolize this observation, one could convolve the received ultrasound signal with each of these GWHPs to gauge the relative strength of the backscatter generated from the three different scattering objects. To minimize correlation between the overlapping GWHP spectra, one could employ more disparate functions for the convolution filtering, for example, $GH_2(t)$ and $GH_8(t)$. An alternative approach is to use a pair of convolution filters to capture the relatively low- and high-frequency information from the backscattered ultrasound signal. Thereafter, one can code the result using RGB color, where R and B are assigned to the low- and high-frequency signal components, respectively, and G is assigned the envelope of the unfiltered backscattered ultrasound signal (*i.e.*, traditional B-scan imaging). This approach helps preserve axial resolution because the convolution filtering has a data smoothing effect.

METHODS

Ultrasound data acquisition

Ultrasound data were acquired using a Vantage 256 programmable scanner equipped with a 128-element L11-4 v linear array transducer (Verasonics, Kirkland, WA, USA). Plane wave imaging was performed at a center frequency of 5 MHz on transmission, and backscattered RF data were quantized at 12 bits and sampled at a rate of 20 MHz. For spatial angular compounding, successively steered and overlapping plane wave transmissions were performed using one, three, five or seven equally spaced angles in the ±18° range. Note the use of a single angle normal to the transducer face is ultrafast plane wave imaging at an angle of 0°. The acoustic output at an image depth of 20 mm was 1.1 MPa, measured using a hydrophone scanning system (AIMS III, Onda, Sunnyvale, CA, USA).

Image processing and spatial angular compounding

All raw RF data had units of millivolts. Two parallel convolution filters were applied to the RF data sequences to measure the relative strength of the received signals relative to $GH_2(t)$ and $GH_8(t)$ after normalization by the signal energy $\sqrt{E_n}$. For each image spatial location, spatial angular compounding is performed by averaging the acquisitions over all steered plane wave transmissions. The
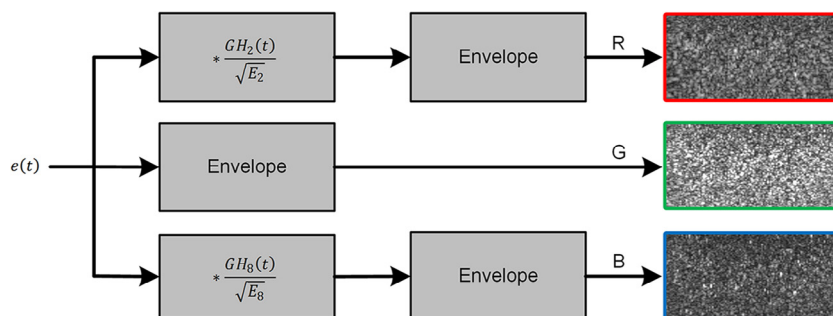
Fig. 1. Schematic diagram highlighting the parallel processing strategy used to generate and display an H-scan image. For a received ultrasound signal $e(t)$, convolution filtering with $GH_2(t)$ and $GH_8(t)$ kernels are performed and assigned *red* and *blue*, respectively, after envelope detection. The envelope of the unfiltered signal is assigned *green* and retains the highest axial resolution.

signal envelope for each of these filtered and compounded data sequences is then calculated using a Hilbert transformation. The relative strength of these filter outputs is color coded whereby the lower-frequency (GH_2) backscatter signals are assigned to the R channel and the higher-frequency (GH_8) components to the B channel. The envelope of the original unfiltered compounded data set is assigned to the G channel to complete the RGB color map and H-scan display image. To help produce a stable real-time H-scan image display, both the R and B channels are normalized to the range from 0 to 1. After histogram analysis of each channel, the 99.95th percentile is set to the maximum value of 1 to help eliminate the spurious outliers. Next, the ratio of the GH_2/GH_8 and GH_8/GH_2 convolution outputs are computed and used to weight the R and B channels, respectively. Lastly, the envelope of the original unfiltered compounded data set is assigned to the G channel, normalized by the maximum value of the R and B channel signals, to complete the RGB color map and H-scan display image. Figure 1 is a schematic diagram summarizing the parallel processing and display of the H-scan image.

Test phantom production

Three soft tissue-mimicking ultrasound test phantoms (length × width × depth of $12 \times 12 \times 8$ cm) were used to test H-scan imaging of different-sized scatterer distributions. Two of these phantom materials were homogeneous, containing different-sized scatterers, and the third phantom was heterogeneous, containing a 13-mm inclusion whereby the background and inclusion contained different-sized microparticles. Homogeneous phantom materials were prepared by heating a 10% gelatin (300 Bloom, Sigma-Aldrich, St. Louis, MO, USA) in degassed water solution to 45°C (Hoyt et al. 2008a, 2008b). Either silica (0.4% concentration, US Silica, Pacific, MO, USA) or polyethylene (0.2% concentration, CoSpheric LLC, Santa Barbara, CA, USA) microspheres were slowly introduced

during constant stirring. The silica microspheres were 15 μm in diameter, whereas the polyethylene microspheres were larger at 75–90 μm in size. All gelatin blocks were placed in a 4°C refrigerator and allowed to cool for at least 12 h before use.

To construct the heterogeneous phantom, the background material was formed using a 10% gelatin solution embedded with 30-μm microspheres (0.25% concentration, US Silica) and a 13-mm cylindrical void positioned in the center of the phantom mold. Once solidified, the void was removed and filled with a second 10% gelatin solution containing smaller 15-μm microspheres (1.0% concentration, US Silica). Given the ultrasound scattering cross section is proportional to the microsphere radius squared, these two concentrations were chosen in attempt to match the acoustic backscatter from each material.

To measure the effects of H-scan spatial angular compounding on the system two-way impulse response (*i.e.*, point-spread function [PSF]), a 200-μm-diameter monofilament nylon string (South End, Northbrook, IL, USA) was suspended in degassed water and imaged at a depth of 20 mm. Anechoic absorbers (Aptflex F28, Precision Acoustics, Dorchester, UK) were used to line the water tank and minimize any reverberation artifacts during ultrasound imaging.

Animal preparation and imaging protocol

Preliminary *in vivo* H-scan imaging studies were performed in tumor-bearing animals ($N = 6$). Briefly, human breast cancer cells (MDA-MB-231, ATCC, Manassas, VA, USA) were maintained in Leibovitz's L-15 medium supplemented with 10% fetal bovine serum. All cells were cultured to approximately 90% confluence before passaging and were grown at 37°C without CO_2 (Heracell 150 i, Thermo Fisher Scientific, Waltham, MA, USA). Appropriate cell numbers were determined using a digital cell counting instrument (Countess II Automated Cell Counter, Thermo Fisher Scientific, USA).

Animal experiments were reviewed and approved by the Institutional Animal Care and Use Committee (IACUC) at the University of Texas at Dallas. Four-week-old female athymic mice (Charles River Laboratories, Wilmington, MA, USA) were implanted orthotopically with 1 million breast cancer cells. Implanted tumors grew for about 3 wk before they were assessed using H-scan imaging. During the ultrasound imaging study, all animals were placed on
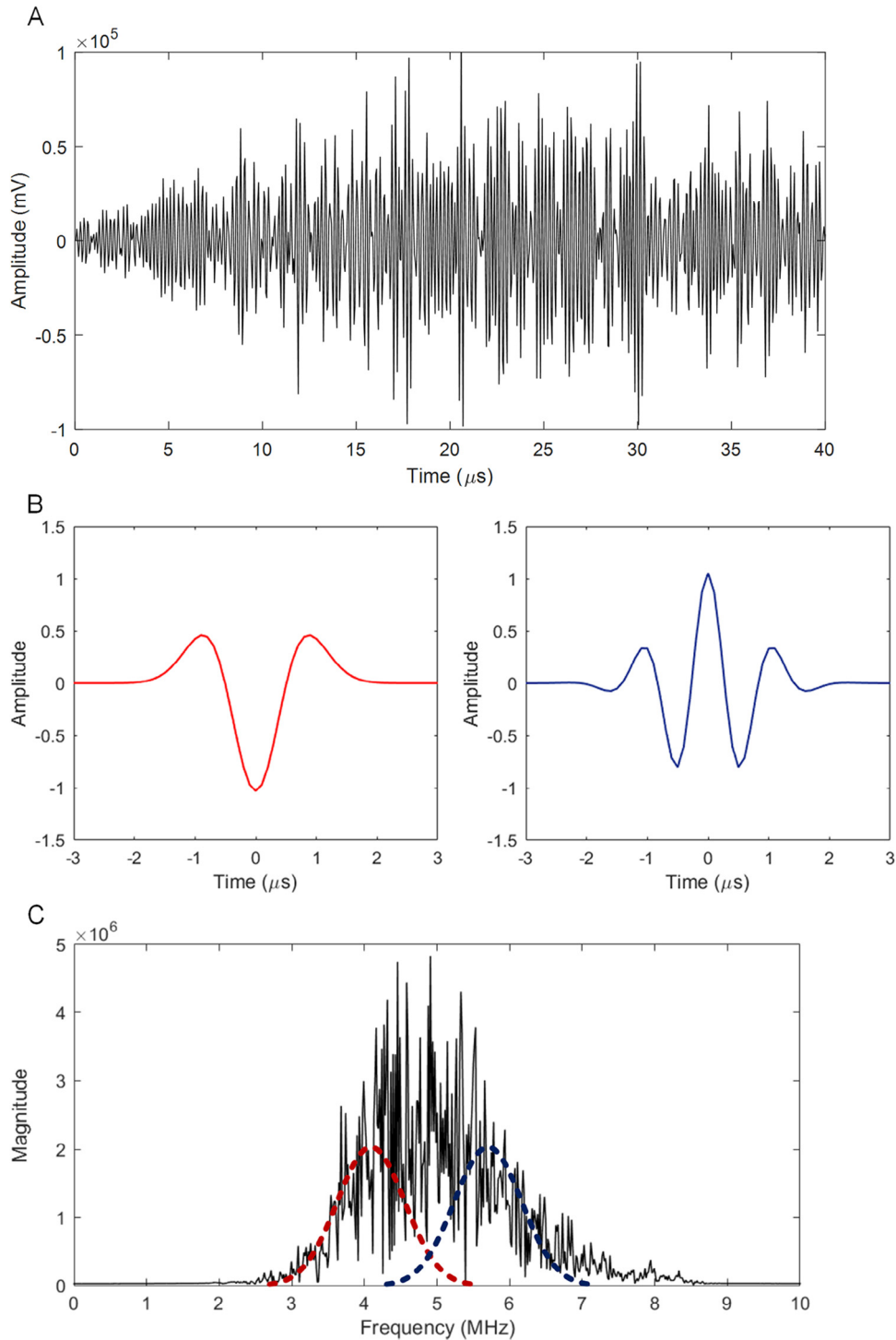

Fig. 2. Representative signal components encountered during H-scan image processing, including a (a) segment of the received backscattered radiofrequency signal, (b) GH_2 (*red*) and GH_8 (*blue*) Gaussian-weighted Hermite polynomials and (c) frequency spectrum of the radiofrequency signal (*black*) and the Gaussian weighted Hermite polynomials bandpass filtering kernels.

a heating pad and controlled with 2% isoflurane anesthesia (Mobile Anesthesia Machine, Parkland Scientific, Coral Springs, FL, USA). Each tumor-bearing animal was imaged at baseline and before receiving an intra-venous injection with the anti-cancer drug Abraxane (25 mg/kg, Celgene, Summit, NJ, USA) *via* a tail vein catheter. Note that the ultrasound transducer was physically fixed over the tumor and the catheter was placed before imaging. This protocol permitted B-scan and H-scan imaging along the exact same tumor cross section before and after injection of the anti-cancer drug to assess any early tumor response and cellular disruption. Imaging was repeated every 30 min for at least 2 h. Thereafter, animals were humanely euthanized *via* cervical dislocation.

Statistical analysis

All data were summarized as means ± standard errors. H-Scan image quality was assessed using a signal-to-noise ratio (SNR) that was computed from a fixed image area as the mean signal divided by the standard deviation. Each statistical measure was computed from the weighted sum of the individual R, G, and B channel components. Variance between multiple measurements was used as an indicator of reproducibility and robustness. An unpaired *t*-test was used to compare B-scan and H-scan imaging SNR results after varying the number of plane waves averaged during spatial angular compounding. A repeated-measures analysis of variance (ANOVA) test was used to assess *in vivo* B-scan and H-scan image group data collected during the pilot animal study. A *p*-value < 0.05 was considered to indicate statistical significance.

RESULTS AND DISCUSSION

A representative backscattered RF data segment and frequency content of $GH_2(t)$ and $GH_8(t)$ filtering kernels are depicted in Figure 2. Although there is some correlation and spectral overlap of the GWHP kernels, they do successfully capture the low- and high-frequency signals encoded in the ultrasound data. These frequency bands are assumed to contain information on relatively large and small scattering objects, respectively.

The impact of H-scan spatial angular compounding on the ultrasound imaging system PSF is summarized in Figure 3. Note the H-scan signal amplitude is calculated from the weighted sum of the R, G and B channel components. Results illustrate a clear improvement in the spatial resolution when incorporating spatial angular compounding during H-scan imaging using plane wave techniques. More specifically, increasing the number of angles progressively decreases the apparent size of the single scatterer. The full width half-maximum (FWHM) of each PSF was found to 6.1, 3.9, 3.4 and 3.6 mm for the one, three, five and seven angles used during compounding, respectively. Relative scatterer size was reduced nearly 1.8 times when using H-scan imaging spatial angular compounding compared with a single plane wave transmission with no compounding. The slight decrease in spatial resolution when going from five to seven angles is noted and attributed to limitations in image sampling and the inability to capture the exact FWHM value. For comparison, the FWHM of each B-scan PSF was found to be 4.3, 3.7, 3.6 and 3.8 mm for the one to seven angles used during compounding, respectively.
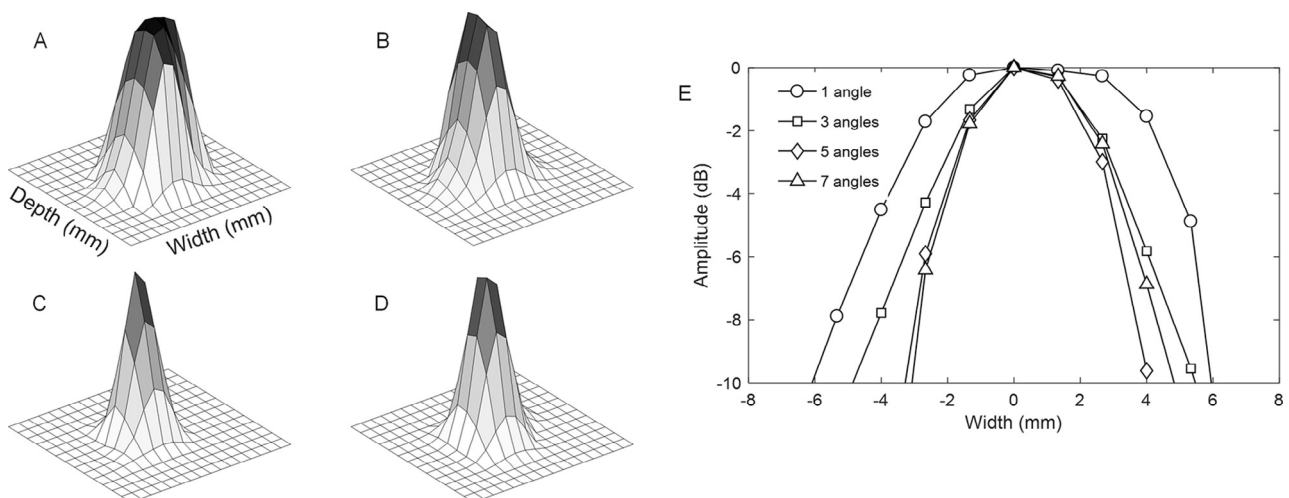

Fig. 3. Impact of H-scan angular compounding on the imaging system point-spread function (PSF). Results depict the spatial PSF for the (a) one, (b) three, (c) five or (d) seven steered plane wave images used during compounding. Transverse line plots are provided in (e) and illustrate improvements in spatial resolution resulting from the incorporation of angular compounding during H-scan imaging using plane wave techniques.
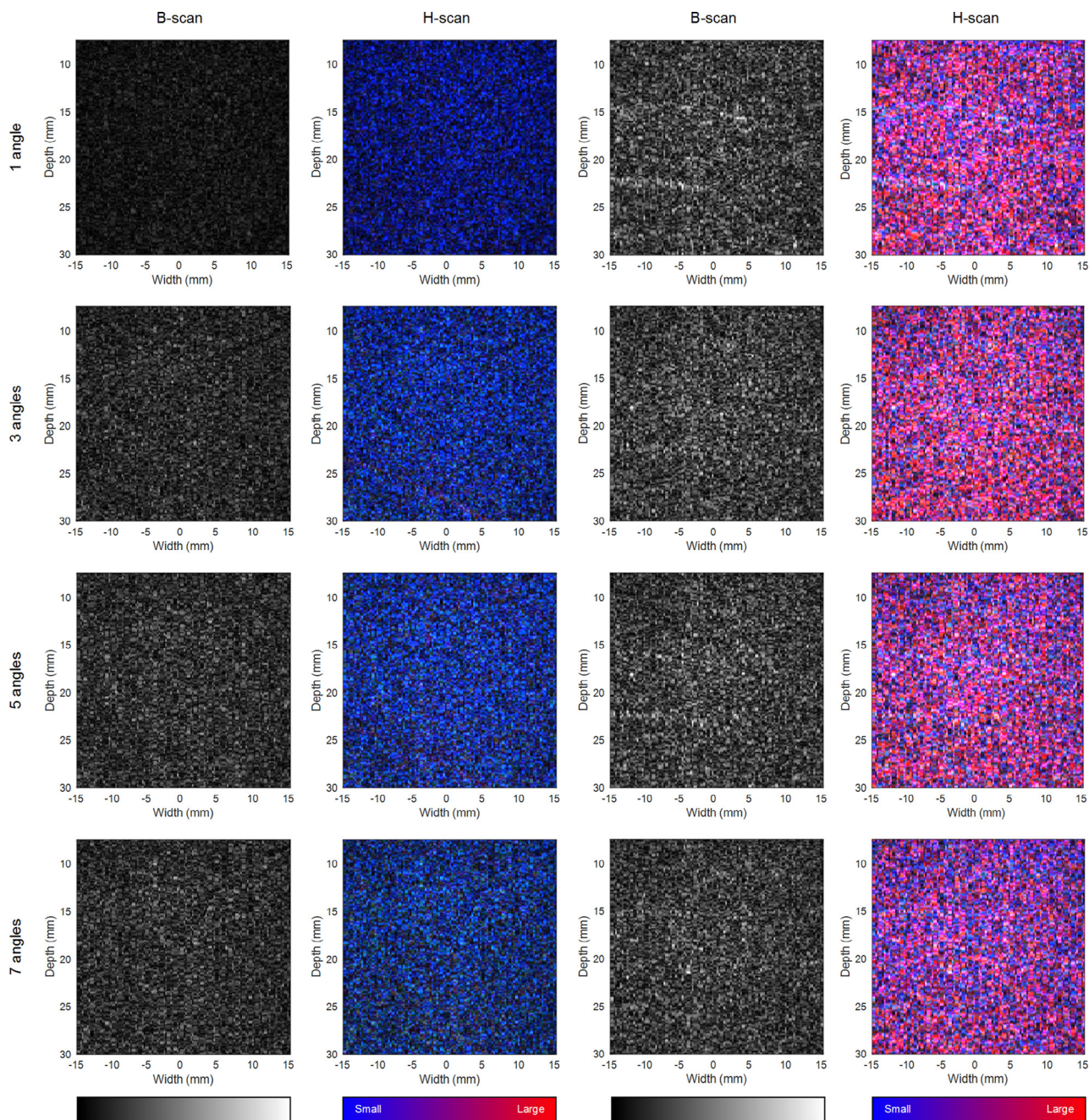
Fig. 4. Ultrasound imaging of homogeneous tissue-mimicking test phantoms containing randomly distributed 15-μm (columns 1 and 2) and 75- to 90-μm (columns 3 and 4) spherical scatterers. Matched B-scan (columns 1 and 3) and H-scan (columns 2 and 4) images are presented as function of the number of steered images used during angular compounding, namely, one, three, five and seven (rows 1 to 4, respectively). The H-scan color map denotes relatively small to large scatterer size in the [0, 1] image amplitude range.

H-Scan imaging was performed using homogeneous tissue-mimicking phantoms containing either small (15 μm) or large (75–90 μm) randomly placed spherical scatterers. A review of the imaging results (Fig. 4) clearly highlights the ability of H-scan to characterize these two different-sized scatterer populations, which is not possible using conventional B-scan imaging alone. To investigate the impact of angular compounding, H-scan imaging data acquired from the phantom material containing the larger scatterers were further analyzed. Taking the ratio of the blue to red channel components throughout the entire image region (after Hilbert transformation and envelope detection),
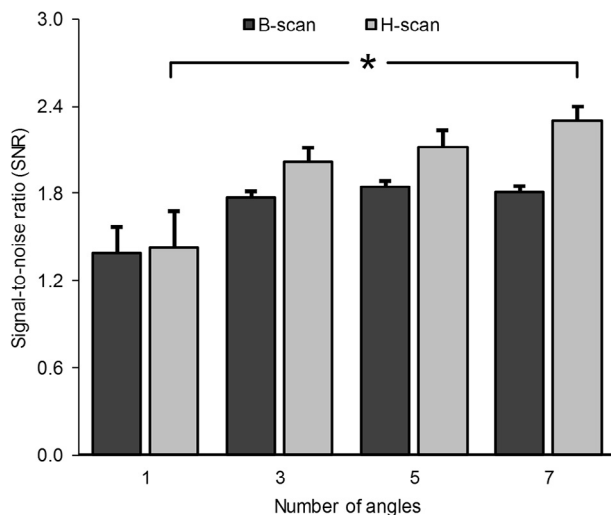
Fig. 5. Summary of signal-to-noise measurements plotted as a function of the number of steered plane wave images averaged during angular compounding. Data were obtained from the spatial analysis of both B-scan and H-scan images collected using a series of homogeneous phantom materials.

mean ratios were 0.90, 1.00, 1.01 and 1.02 dB for the one, three, five and seven angles used during compounding, respectively. These findings indicate there is a blue shift in the H-scan color display that suggests the apparent size of the ultrasound scattering objects has decreased. Note this observation is confirmed by the two-way PSF measurements in Figure 3. Given the use of ultrasound plane waves to construct the H-scan images, the findings appear spatially homogeneous, which is attributed to the uniformity of the acoustic field on transmission. Conversely, focused ultrasound techniques used for H-scan imaging can exhibit decreased resolution and image quality away from the focal zone depth (*i.e.*, PSF spreading).

Signal-to-noise ratio measurements obtained from the spatial analysis of both B-scan and H-scan images collected using a series of homogeneous phantom materials (containing 15-µm-sized scatterers) are summarized in Figure 5. In general, these findings further highlight the progressive improvement in image quality as the number of steered plane wave images used during B-scan ($p < 0.41$) and H-scan ($p < 0.012$) spatial angular compounding is increased from one to seven. Although the data are not presented herein, increasing the number of angles beyond seven did not further improve our imaging results. We hypothesize that because we limited all steered plane wave transmissions to the ±18° range, increasing the number of steered plane wave images within that space increases the correlation between the images to be averaged. Spatial compounding is most effective when signals to be averaged are uncorrelated (Chen et al. 2005). Notwithstanding, when ultrasound scatterers are densely distributed and of sufficient

number, the RF backscattered signals obey Gaussian statistics while the envelope of the signal follows a Rayleigh distribution (Wagner et al. 1988). Thus, the SNR is theoretically fixed at 1.91 in B-scan images, which is in good agreement with our findings.

Next, H-scan imaging was performed using a heterogeneous tissue-mimicking phantom containing both small (15 µm, background material) and large (30 µm, inclusion material) spherical scatterers (Fig. 6). Inspection of these results clearly reveals the different-sized scatterer distributions. The ultrasound images again appear to improve when incorporating spatial angular compounding. Future phantom studies will investigate direct measurements of scatterer size and concentration and impact on H-scan image quality (*i.e.*, R and B channel signal magnitude).

Breast tumor–bearing mice were imaged using H-scan with angular compounding (five steered plane wave angles) before and after administration of the anti-cancer drug Abraxane. Representative B-scan and H-scan image sequences at baseline and 30, 60 and 120 min after drug dosing are provided in Figure 7. Inspection of theses ultrasound images suggests a progressive reduction in both the B-scan and H-scan image amplitudes. Intra-tumoral measurements from each animal were averaged, and the group summary is detailed in Figure 8. These results further reveal a progressive decrease in both repeated H-scan and B-scan image measurements, albeit not statistically significant ($p > 0.25$). Notwithstanding, there was a considerable change in the mean H-scan image intensity (compared with baseline measurements) at the terminal 120-min time point ($30.5 \pm 12.4\%$, $p = 0.17$). At this same time point, there was also a decrease in the B-scan image intensity ($14.2 \pm 9.9\%$, $p = 0.38$). Given Abraxane is a class of chemotherapeutics that inhibit cellular mitosis, leading to apoptosis, we theorize that the discernible color map shift observed in the H-scan image sequences is detection of cancer cell shrinkage as it undergoes apoptotic cell death (Elmore 2007). Both *in vitro* and *in vivo* studies have revealed that apoptosis occurs in cancer cells within hours after exposure to paclitaxel and consistent with our hypothesis (Orth et al. 2011). This shrinkage manifests as a decrease in the scattering cross section of the affected cells and may also help explain the decrease in the B-scan signal. Future work will investigate this phenomenon in more detail with appropriate controls and correlate H-scan imaging results with immunohistological findings from excised tumor tissue sections.

CONCLUSIONS

H-Scan is a new ultrasound-based imaging technique that locally estimates the relative size and spatial distribution of acoustic scattering objects. As we
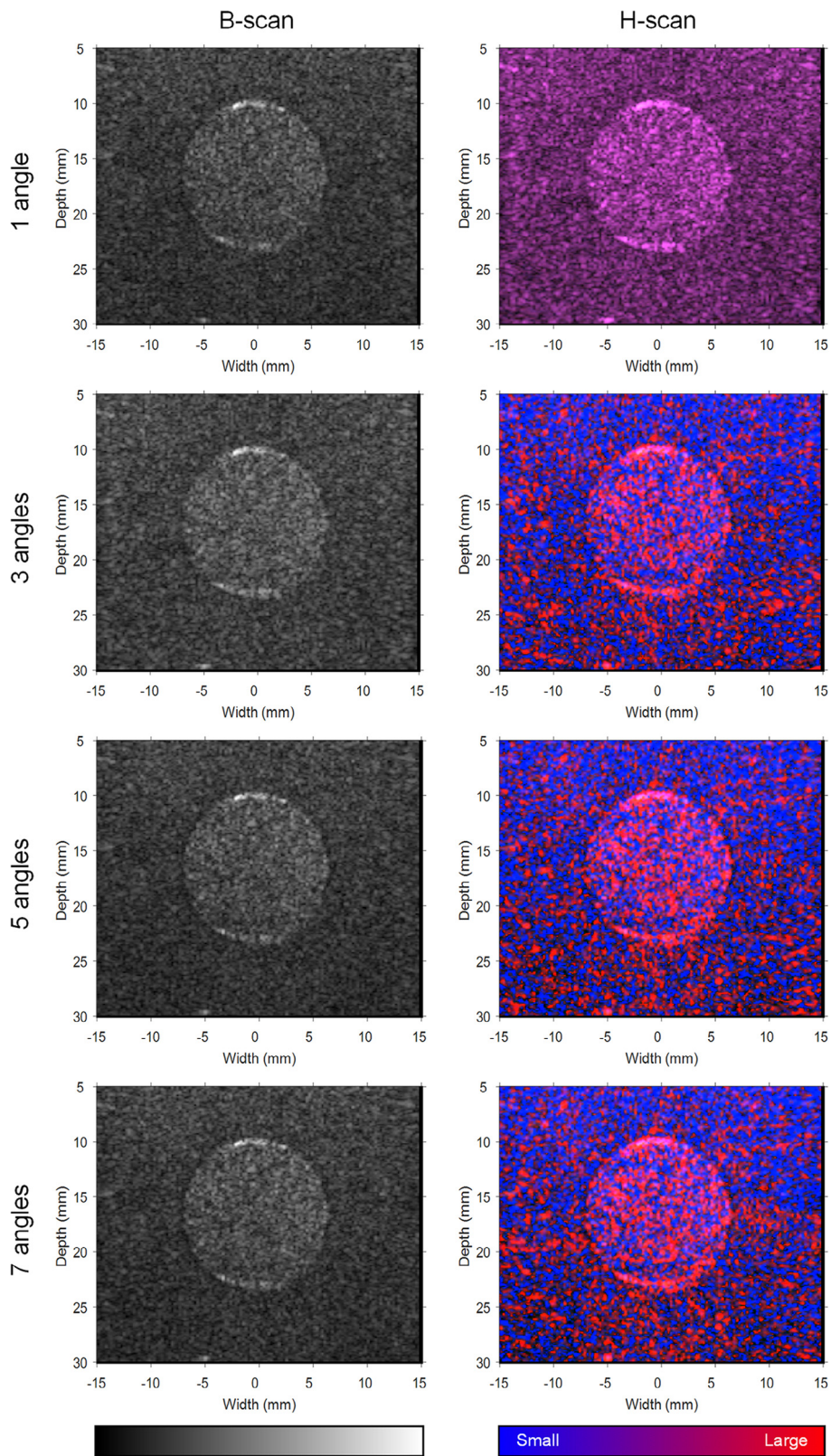
Fig. 6. Ultrasound imaging of heterogeneous tissue-mimicking test phantoms containing randomly distributed 15-µm (background) and 30-µm (inclusion) spherical scatterers. Matched B-scan (left) and H-scan (right) images are presented as a function of the number of steered images used during angular compounding, namely, one, three, five and seven (top to bottom, respectively).
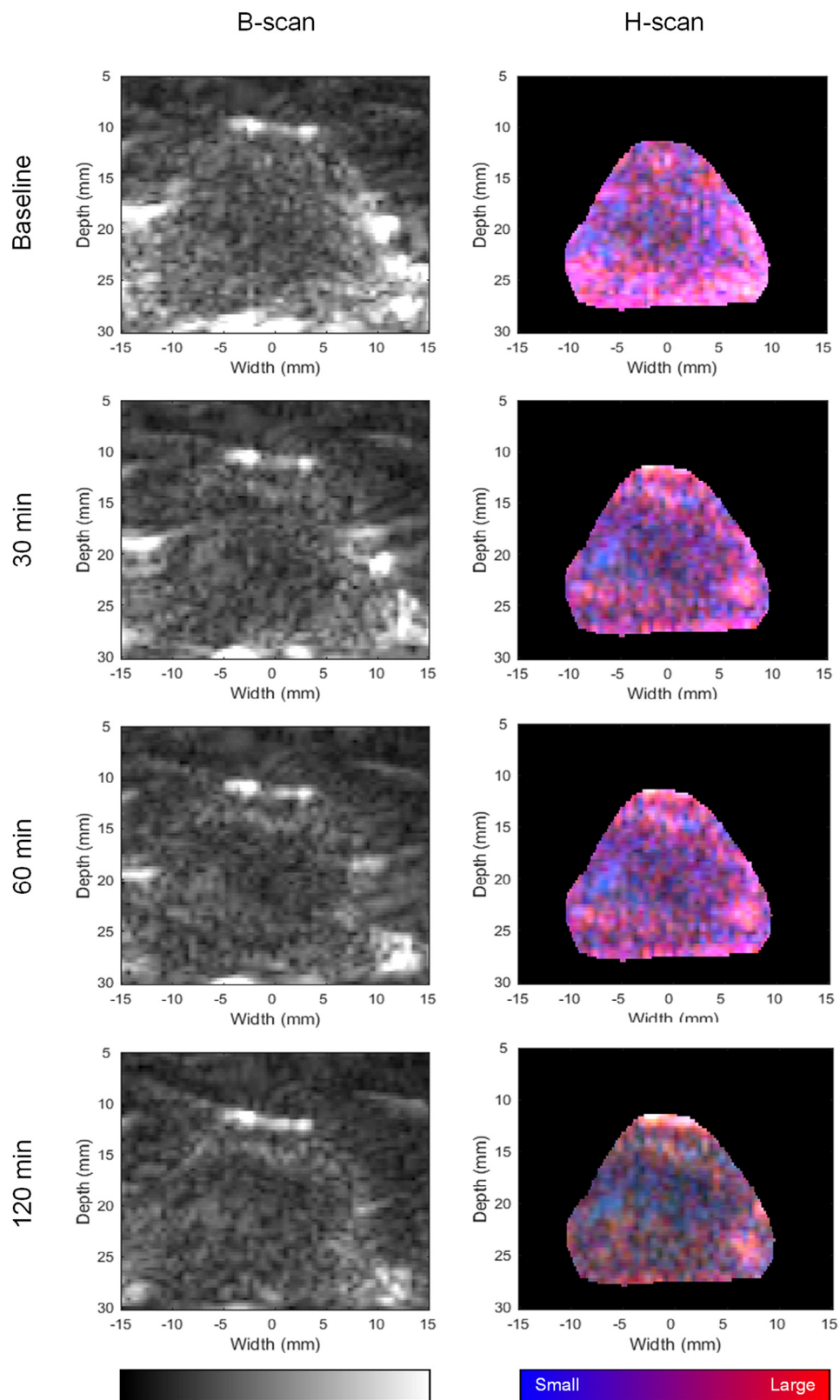
B-scan

H-scan

Fig. 7. Ultrasound results from *in vivo* imaging of a breast tumor-bearing animal. Matched B-scan (left) and segmented H-scan (right) images are presented for baseline (0 min), 30 min, 60 min and 120 min (top to bottom, respectively) after systemic administration of a chemotherapeutic drug (Abraxane). Note the progressive shift in the H-scan image intensity which may be an early indicator of tumor response to the anti-cancer treatment.
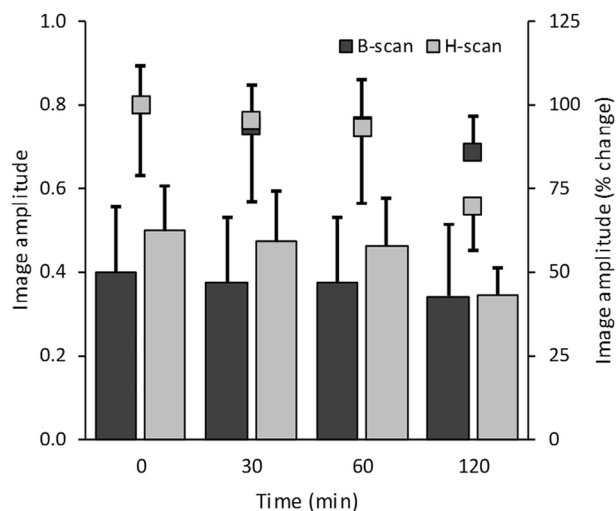
Fig. 8. Summary of B-scan and H-scan results obtained from *in vivo* imaging of breast tumor-bearing animals before and after systemic administration of a chemotherapeutic drug. Group data describe measurements of the mean ultrasound image amplitude in tumor tissue (left vertical scale and bar graph) and percentage changes relative to baseline measures (right vertical scale and scatterplot).

successfully illustrated, H-scan imaging can be implemented on a programmable ultrasound scanner and using plane wave techniques. Image quality can be significantly improved when using steered plane wave transmissions and spatial angular compounding compared with no compounding. Overall, the preliminary examples presented suggest that H-scan imaging is a promising tissue characterization modality. Furthermore, H-scan may provide prognostic value during monitoring of the early tumor response (or lack thereof) to anti-cancer treatment, and more research is warranted.

REFERENCES

Bridal SL, Wallace KD, Trousil RL, Wickline SA, Miller JG. Frequency dependence of acoustic backscatter from 5 to 65 MHz (0.06 < ka < 4.0) of polystyrene beads in agarose. J Acoust Soc Am 1996;100: 1841–1848.

Chen JF, Zagzebski JA, Madsen EL. Tests of backscatter coefficient measurement using broadband pulses. IEEE Trans Ultrason Ferroelectr Freq Control 1993;40:603–607.

Chen Q, Gerig AL, Techavipoo U, Zagzebski JA, Varghese T. Correlation of RF signals during angular compounding. IEEE Trans Ultrason Ferroelectr Freq Control 2005;52:961–970.

Couture O, Fink M, Tanter M. Ultrasound contrast plane wave imaging. IEEE Trans Ultrason Ferroelectr Freq Control 2012;59:2676–2683.

Doherty JR, Trahey GE, Nightingale KR, Palmeri ML. Acoustic radiation force elasticity imaging in diagnostic ultrasound. IEEE Trans Ultrason Ferroelectr Freq Control 2013;60:685–701.

Elmore S. Apoptosis: A review of programmed cell death. Toxicol Pathol 2007;35:495–516.

Gennisson JL, Deffieux T, Fink M, Tanter M. Ultrasound elastography: Principles and techniques. Diagn Interv Imaging 2013;94:487–495.

Hall CS, Verdonk ED, Wickline SA, Perez JE, Miller JG. Anisotropy of the apparent frequency dependence of backscatter in formalin fixed human myocardium. J Acoust Soc Am 1997;101:563–568.

Hoyt K, Castaneda B, Parker KJ. Two-dimensional sonoelastographic shear velocity imaging. Ultrasound Med Biol 2008a;34:276–288.

Hoyt K, Forsberg F, Ophir J. Analysis of a hybrid spectral strain estimation technique in elastography. Phys Med Biol 2006;51:197–209.

Hoyt K, Kneezel T, Castaneda B, Parker KJ. Quantitative sonoelastography for the in vivo assessment of skeletal muscle viscoelasticity. Phys Med Biol 2008b;53:4063–4080.

Kolios MC, Czarnota GJ, Lee M, Hunt JW, Sherar MD. Ultrasonic spectral parameter characterization of apoptosis. Ultrasound Med Biol 2002;28:589–597.

Lizzi FL, Astor M, Feleppa EJ, Shao M, Kalisz A. Statistical framework for ultrasonic spectral parameter imaging. Ultrasound Med Biol 1997;23:1371–1382.

Macovski A. Medical imaging systems. Englewood Cliffs, NJ: Prentice Hall; 1983.

Madsen EL, Insana MF, Zagzebski JA. Method of data reduction for accurate determination of acoustic backscatter coefficients. J Acoust Soc Am 1984;76:913–923.

Oelze ML, Mamou J. Review of quantitative ultrasound: Envelope statistics and backscatter coefficient imaging and contributions to diagnostic ultrasound. IEEE Trans Ultrason Ferroelectr Freq Control 2016;63:336–351.

Oelze ML, O'Brien WD. Method of improved scatterer size estimation and application to parametric imaging using ultrasound. J Acoust Soc Am 2002;112:3053–3063.

Orth JD, Kohler RH, Foijer F, Sorger PK, Weissleder R, Mitchison TJ. Analysis of mitosis and antimitotic drug responses in tumors by in vivo microscopy and single-cell pharmacodynamics. Cancer Res 2011; 71:4608–4616.

Parker KJ. Scattering and reflection identification in H-scan images. Phys Med Biol 2016a;61:L20–L28.

Parker KJ. The H-scan format for classification of ultrasound scattering. OMICS J Radiol 2016b;5:1–7.

Parker KJ, Doyley MM, Rubens DJ. Imaging the elastic properties of tissue: The 20 year perspective. Phys Med Biol 2011;56:R1–R29.

Poularikas A. Transforms and applications handbook. Boca Raton, FL: CRC Press; 2010.

Romijn RL, Thijssen JM, van Delft JL, de Wolff-Rouendaal D, van Best J, Oosterhuis JA. In vivo ultrasound backscattering estimation for tumour diagnosis: An animal study. Ultrasound Med Biol 1989;15: 471–479.

Szabo TL. Diagnostic ultrasound imaging: Inside out. Boston: Academic Press; 2014.

Tanter M, Fink M. Ultrafast imaging in biomedical ultrasound. IEEE Trans Ultrason Ferroelectr Freq Control 2014;61:102–119.

Thijssen JM. Ultrasonic tissue characterisation and echographic imaging. Phys Med Biol 1989;34:1667–1674.

Thomas LJ, Barzilai B, Perez JE, Sobel BE, Wickline SA, Miller JG. Quantitative real-time imaging of myocardium based on ultrasonic integrated backscatter. IEEE Trans Ultrason Ferroelectr Freq Control 1989;36:466–470.

Wagner RF, Insana MF, Smith SW. Fundamental correlation lengths of coherent speckle in medical ultrasonic images. IEEE Trans Ultrason Ferroelectr Freq Control 1988;35:34–44.